IFASD 2015
International Forum on Aeroelasticity and Structural Dynamics
June 28 — July 02, 2015 ▲ Saint Petersburg, Russia

# LOW-FIDELITY 2D ISOGEOMETRIC AEROELASTIC OPTIMIZATION WITH APPLICATION TO A MORPHING AIRFOIL

**Erik Gillebaart**[1], **Roeland De Breuker**[1]

[1] Delft University of Technology
Kluyverweg 1, 2629 HS Delft, The Netherlands
E.Gillebaart@tudelft.nl

**Keywords:** Low-fidelity aeroelasticity, isogeometric analysis, morphing airfoil, potential flow, curved Timoshenko beams

**Abstract:** Low-fidelity isogeometric aeroelastic analysis has not received much attention since the introduction of the isogeometric analysis (IGA) concept, while the combination of IGA and the boundary element method in the form of the potential flow theory shows great potential. This paper presents a two-dimensional low-fidelity aeroelastic optimization framework consisting of a loosely coupled isogeometric potential flow model and isogeometric curved Timoshenko beam model. Application of the framework to the optimization of the landing performance for an active morphing airfoil shows its potential, although the absence of viscosity in the aerodynamic model has a detrimental effect.

## 1 INTRODUCTION

Isogeometric analysis has captured the attention of many researchers in the past decade. The principle of isogeometric analysis, introduced in 2005 [1], is to apply basis functions that are typically used in computer aided design (CAD) to the analysis as well, instead of the conventional polynomial basis functions. The main benefit of this approach is that the step from CAD geometry to an analysis suitable geometry is largely circumvented, since the CAD geometry can directly be used in the analysis. This also greatly simplifies mesh refinement and degree elevation, as the coarsest mesh is already the exact geometry.

The application of IGA in the field of aeroelasticity and fluid-structure interaction (FSI) has been limited so far and is usually focused on high-fidelity modeling. Some of the applications include FSI of wind turbines [2–4] and blood flows [5, 6]. Low-fidelity aeroelastic analysis has been almost untouched to the author's knowledge, while, for example, aerodynamic analysis in the form of the boundary element method (BEM) has been shown to be a suitable candidate for the implementation of IGA. [7–9]

The fact that the BEM only requires a boundary description of the problem creates a perfect match with CAD, since the output of such software is only a boundary discretization. Furthermore, analyzing the exact geometry is beneficial for aerodynamic analysis, since small perturbations can have significant effects. Also in other fields, such as acoustics[10] and elastostatics [11–13], it has been shown that the benefits of IGA work well in a BEM framework.

Another advantage of IGA is that it is very suitable for shape optimization problems, especially in a BEM framework, as has been shown for structural shape optimization. [11] The IGA implementation delivers very accurate shape sensitivities, resulting in precise optimization results. Furthermore, the discretization can be immediately used in optimization, removing the need for a separate shape parameterization. [14]

All these benefits of IGA have lead to the idea of implementing the concept into a low-fidelity aeroelastic framework with the purpose of performing simultaneous shape and stiffness optimization of composite wings during the preliminary design phase. The performance increase resulting from this simultaneous optimization has been shown already using high-fidelity aeroelastic frameworks [15], but these are computationally expensive, making them less attractive for the early design stages.

As a first step, this paper presents a two-dimensional low-fidelity aeroelastic framework based on the IGA concept. An IGA potential flow solver is loosely coupled to an IGA curved Timoshenko beam solver. A gradient-based optimizer is used in combination with analytically computed sensitivities. To show the capabilities of the framework, it is applied to the aeroelastic optimization of an active morphing airfoil.

The paper is built up as follows. In section 2 a short introduction into IGA is given, and the aerodynamic and structural model are described. The coupling of the models is also explained. The next section presents the design case of the morphing airfoil, together with the optimization specifications. The results are presented and discussed in section 4 and the paper is concluded in section 5.

## 2 METHODOLOGY

The low-fidelity aeroelastic framework consists of an isogeometric potential flow aerodynamic model and an isogeometric curved Timoshenko beam structural model. This section will describe the theory and implementation of both these models. The coupling between these models and the loads and displacements transfer method will also be presented. First a short introduction into NURBS and isogeometric analysis is given for completeness.

### 2.1 NURBS curves and basis functions

In the present work NURBS basis functions are used, because these are the most common in CAD software. A NURBS curve is fully defined by three items:

- The control points $\mathbf{P}_i \in \mathbb{R}^d, 1 \le i \le n$, where $d$ indicates the dimensionality of the problem.
- The degree $p$ of the basis functions.
- The knot vector $\Xi = [\xi_1, \xi_2, ..., \xi_{n+p+1}]$.

An example of a two-dimensional NURBS curve of degree 3 is shown in Figure 1.

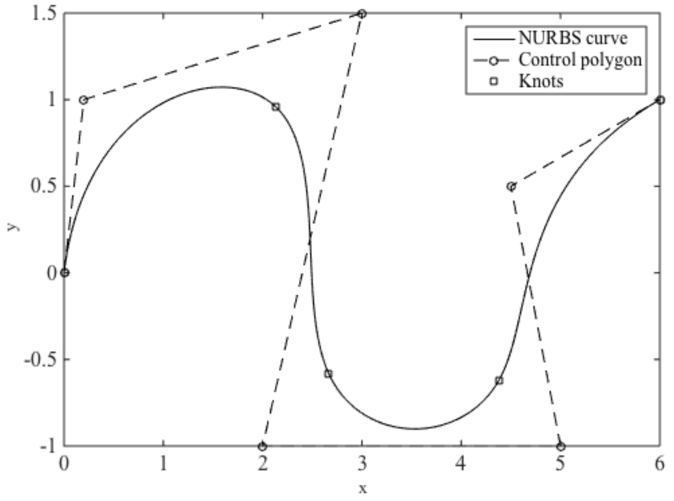

Figure 1: Example of a NURBS curve with control polygon and knot location

From this example it can be seen that the control point may or may not be on the curve. Only so-called open knot vectors are used in the present work, meaning that the first and last knots are repeated $p$+1 times. As a consequence the NURBS curve is always interpolatory at the start and end of the curve. The order of continuity of the rest of the curve can be modified by repeating the other knots. The order of continuity at a knot is equal to $p+1-r$, where $r$ is the multiplicity of this knot.

Mathematically a NURBS curve can be represented as follows:

$$\mathbf{C}(\xi)=\sum_{i=1}^{n}R_{i,p}(\xi)\mathbf{P}_i, \tag{1}$$

where $\mathbf{C}(\xi)$ is the vector with Cartesian coordinates of the point described by the parametric point $\xi$, and $R_{i,p}(\xi)$ is the $i^{th}$ rational basis functions of degree $p$. These basis functions are given by

$$R_{i,p}(\xi)=\frac{N_{i,p}(\xi)w_i}{\sum_{j=1}^{n}N_{j,p}(\xi)w_j}, \tag{2}$$

where $N_{i,p}(\xi)$ is a B-spline basis function of order $p$, and $w_i$ is the weight factor corresponding to the $i^{th}$ control point. The B-spline basis functions of degree 0 are defined as

$$N_{a,0}(\xi)=\begin{cases}1 & \text{if } \xi_i \le \xi \le \xi_{i+1}\\ 0 & \text{otherwise}\end{cases} \tag{3}$$

and for higher degrees

$$N_{i,p}(\xi)=\frac{\xi-\xi_i}{\xi_{i+p}-\xi_i}N_{i,p-1}(\xi)+\frac{\xi_{i+p+1}-\xi}{\xi_{i+p+1}-\xi_{i+1}}N_{i+1,p-1}(\xi) \tag{4}$$

The recursive character results in higher cost for computing the basis functions. However, several efficient algorithms exist to speed up the computations, of which the Cox-de-Boor algorithm [16] is most popular. This algorithm was also used in this work.

NURBS basis functions (as well as B-spline basis functions) possess some properties that are favorable for their implementation into analysis models. The basis functions possess the local support property, meaning that in every knot span $[\xi_i, \xi_{i+1})$ at most $p$+1 non-zero basis functions exist, namely $N_{i-p,p},\ldots,N_{i,p}$. Furthermore, they are non-negative and form a partition of unity at each parametric location. In the interior of the knot span all derivatives of the non-zero basis functions exist and at a knot itself the functions are $p$-$r$ times continuously differentiable.

The principle of IGA, as was mentioned before, is to use the NURBS basis functions both for describing the geometry and to approximate the unknowns. For the aerodynamic model the unknowns are the doublet strength, as will be explained in section 2.2, and for the structural model the unknowns are the displacements, as will be explained in section 2.3. The power in this approach lies in the fact that the geometry and its boundary discretization can be completely done in CAD software and this geometry can immediately be analyzed in the IGA analysis software.

Even though the exact geometry is provided by the CAD software, the discretization might not be detailed enough to enable the analysis to provide accurate results. This problem can be easily solved by either knot refinement or degree elevation, or a combination of both. [17] The computational algorithms to perform such operations on NURBS functions are well documented in literature. [16] The knot refinement and degree elevation operations have no effect on the geometry itself, making these operations efficient and simple.

### 2.2 Aerodynamic model

The aerodynamic model is based on the potential flow model, which is characterized by Laplace’s equation:

$$\nabla^2 \Phi^* = 0, \tag{5}$$

where $\Phi^*$ is the total velocity potential. The boundary conditions for the flow over an airfoil are the flow tangency condition at the boundary of the airfoil and that the disturbance of the flow should go to zero far away from the airfoil:

$$\frac{\partial \Phi^*(\mathbf{x})}{\partial \mathbf{n}} = 0 \quad \text{for } \mathbf{x} \in \Gamma_b, \tag{6}$$

$$\lim_{r\to\infty} \nabla \Phi = 0, \tag{7}$$

where $\mathbf{n}$ is the outward unit normal vector to the boundary of the body $\Gamma_b$, and $\Phi$ is the perturbation velocity potential. This problem is reduced to solving the following boundary integral equation (BIE):[18]

$$C(\mathbf{x}_0)\Phi(\mathbf{x}_0) = \int_{\Gamma_b} \left( \frac{\partial \Phi}{\partial \mathbf{n}} G - \Phi \frac{\partial G}{\partial \mathbf{n}} \right) dS - \int_{\Gamma_w} \Delta\Phi \frac{\partial G}{\partial \mathbf{n}} dS \tag{8}$$

where C denotes the jump term, $\Gamma_w$ the wake surface, and G the fundamental solution as is given in equation (9).

$$G(\mathbf{x}_0, \mathbf{x}) = \frac{1}{2\pi} \log\left( \frac{1}{|\mathbf{x}_0 - \mathbf{x}|} \right) \tag{9}$$

The normal derivative of the fundamental solution is given by

$$\frac{\partial G}{\partial \mathbf{n}}(\mathbf{x}_0,\mathbf{x}) = \frac{(\mathbf{x}_0-\mathbf{x})\cdot\mathbf{n}(\mathbf{x})}{2\pi\left|\mathbf{x}_0-\mathbf{x}\right|^2}. \tag{10}$$

Setting the normal derivative of the perturbation potential to zero, gives the following solution:

$$C(\mathbf{x}_0)\Phi(\mathbf{x}_0) = -\int_{\Gamma_b} \Phi\frac{\partial G}{\partial \mathbf{n}}dS - \int_{\Gamma_w} \Delta\Phi\frac{\partial G}{\partial \mathbf{n}}dS \tag{11}$$

When the point **y** approaches point **x** on the boundary of the body a singularity will be encountered. To desingularize equation (11), the potential inside the body is investigated. The flow tangency boundary condition in equation (6) implies that the potential inside the body is constant. Furthermore, the normal vector is opposite compared to that of the external problem and the jump term becomes 1-$C$(**x**) [19]. The following equation thus holds for the interior problem:

$$1 - C(\mathbf{x}_0) = -\int_{\Gamma_b} \frac{\partial G}{\partial \mathbf{n}}dS \tag{12}$$

This relation is fully dependent on the geometry of the problem. Multiplying the equation with the total potential at point $\mathbf{x}_0$ and subtracting it from equation (11) gives

$$\Phi(\mathbf{x}_0) = \int_{\Gamma_b} \left(\Phi(\mathbf{x}) - \Phi(\mathbf{x}_0)\right)\frac{\partial G}{\partial \mathbf{n}}dS, \tag{13}$$

which is no longer singular. Combining equation (11) and (13) and introducing the free stream potential $\Phi_\infty$, gives the equation for the total velocity potential:

$$\Phi^*(\mathbf{x}_0) = -\int_{\Gamma_b} \left(\Phi(\mathbf{x}) - \Phi(\mathbf{x}_0)\right)\frac{\partial G}{\partial \mathbf{n}}dS - \int_{\Gamma_w} \Delta\Phi\frac{\partial G}{\partial \mathbf{n}}dS + \Phi_\infty \tag{14}$$

For the internal problem the constant velocity potential is set to zero, which results in the final form of the problem that needs to be solved to find the velocity potential along the boundary:

$$-\int_{\Gamma_b} \left(\Phi(\mathbf{x}) - \Phi(\mathbf{x}_0)\right)\frac{\partial G}{\partial \mathbf{n}}dS - \int_{\Gamma_w} \Delta\Phi\frac{\partial G}{\partial \mathbf{n}}dS + \Phi_\infty = 0 \tag{15}$$

The velocity potential jump in the wake is related to the unknown velocity potential distribution on the body through the Kutta condition.[20]

The geometry is now discretized using a NURBS curve and the unknown doublet strength is approximated using the same basis functions.

$$\mathbf{x}(\xi) = \sum_{i=1}^{n} R_{i,p}(\xi)\mathbf{P}_i; \qquad \Phi(\xi) \approx \sum_{i=1}^{n} R_{i,p}(\xi)\Phi_i \tag{16}$$

Using the dot to indicate derivatives with respect to $\xi$ to simplify notation, the Jacobian of the transformation from the Cartesian coordinate system to the parametric space becomes

$$J(s) = \dot{s} = \sqrt{\dot{x}_1^2 + \dot{x}_2^2}, \tag{17}$$

The non-zero knot spans in the knot vector of the curve can be considered as the elements that build up the geometry. The collocation method is used to set up a linear system of $n$ equations for the $n$+1 unknown velocity potentials. The final equation is provided by the Kutta condition. The resulting system is as follows:

$$\begin{bmatrix} H_{1,1} & \cdots & H_{1,n} & H_{1,n+1} \\ \vdots & \ddots & \vdots & \vdots \\ H_{n,1} & \cdots & H_{n,n} & H_{n,n+1} \\ -1 & 0 & 1 & -1 \end{bmatrix} \begin{bmatrix} \Phi_1 \\ \vdots \\ \Phi_n \\ \Delta\Phi \end{bmatrix} = \begin{bmatrix} \Phi_\infty^1 \\ \vdots \\ \Phi_\infty^n \\ 0 \end{bmatrix} \tag{18}$$

where $H_{i,j}$ are the aerodynamic influence coefficients. The wake is modeled as a single element with a constant value, so its influence can be computed analytically. The other, non-singular, influence coefficients are computed numerically in the parametric domain. The integrals as given in equation (19), are computed using standard Gaussian quadrature.

$$H_{i,j} = \int_0^1 R_{j,p}(\xi) \frac{\partial G(\xi_i, \xi)}{\partial \mathbf{n}} J \, d\xi \tag{19}$$

The desingularized contributions are computed by summing up the non-singular contributions and multiply it with the basis function values in the collocation point.

Once equation (18) has been solved for the velocity potential, the lift coefficient can immediately be determined from the potential jump in the wake:

$$C_l = \frac{-\rho Q_\infty \Delta\Phi}{\frac{1}{2}\rho Q_\infty^2 c} = \frac{-2\Delta\Phi}{Q_\infty c}, \tag{20}$$

where $Q_\infty$ is the free stream velocity, $\rho$ the air density and $c$ the chord length.

To find the pressure distribution over the airfoil the flow velocity tangential to the airfoil boundary has to be found. This is found by taking the derivative of the doublet strength in the tangential direction. In conventional panel methods the derivative has to approximated using a finite difference scheme, but since the NURBS curve representing the doublet strength is easily differentiable this can be done exactly:

$$Q_t = \frac{d\Phi}{ds} = \frac{1}{J}\frac{d\Phi}{d\xi} \tag{21}$$

The pressure distribution is now found using equation

$$p = -\frac{\rho}{2}\left(Q_t^2 - Q_\infty^2\right) \tag{22}$$

For the transfer of the pressure to the structure it is convenient to have the pressure distribution in the form of a NURBS curve. The derivative of a NURBS curve, however, is no longer a NURBS curve. The squared tangential velocity is thus evaluated at a number of points along the boundary and a NURBS curve is fitted through this data to end up with a NURBS curve again.

### 2.3 Structural model

The structural model is based on linear curved Timoshenko beams using an isogeometric formulation. Most existing work in this field makes use of the local Frenet coordinate system to formulate the beam model. [21, 22] In the present framework a global coordinate system was required to enable the transfer of loads from the aerodynamic model to the structural model and the displacements the other way around. For clarity first the formulation in the Frenet coordinate system is described, followed by the modifications that are required to obtain a formulation in the global coordinate system.

### 2.3.1 Local formulation

In the Frenet coordinate system, defined by the tangential, normal and bi-normal unit vectors (**t**, **n**, **b**), the membrane, transverse shear and bending strain components of a planar curved beam are defined as

$$\varepsilon_m(s) = \frac{du_t(s)}{ds} - \frac{u_n(s)}{R(s)}, \tag{23}$$

$$\gamma_s(s) = \frac{u_t(s)}{R(s)} + \frac{du_n(s)}{ds} - \theta_b(s), \tag{24}$$

$$\chi_b(s) = \frac{d\theta_b(s)}{ds}, \tag{25}$$

where $u_t$, $u_n$ and $\theta_b$ are the midline tangential and normal displacements, and the cross-section rotation, respectively. They are all expressed in the curvilinear coordinate $s$, as shown in Figure 2.

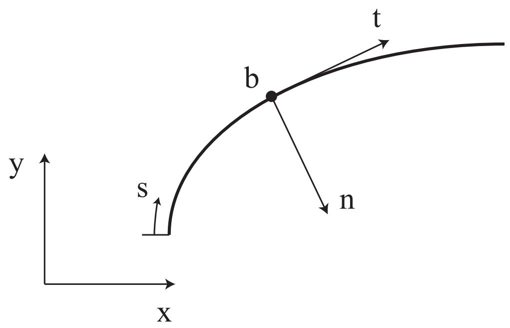

Figure 2: Curved beam coordinate systems

The total potential energy of the planar Timoshenko beam is the sum of the elastic strain energy $U$, and the potential energy of applied external forces $V$:

$$\Pi = U + V, \tag{26}$$

$$U = \frac{1}{2}\int_0^L \left( EA\varepsilon_m^2 + GA\gamma_s^2 + EI\theta_b^2 \right) ds, \tag{27}$$

$$V = -\int_0^L (\mathbf{f} \cdot \mathbf{u}) ds - \mathbf{F} \cdot \mathbf{u}, \tag{28}$$

where $E$ and $G$ are the Young's modulus and shear modulus respectively, $A$ is the cross-sectional area and $I$ is the moment of inertia along **b**. The vectors **F**, **f** and **u** are the concentrated loads, distributed loads, and displacements and rotations, respectively.

The IGA implementation starts with the representation of the geometry using NURBS curves. For simplicity the explanation will first be given for a geometry built up out of a single NURBS curve (single patch). The required modifications for a multi-patch geometry will be described later. The geometry is described by equation (29), where the control points $\mathbf{P}_i$ contain the $x$ and $y$ coordinates.

$$\mathbf{x}(\xi)=\sum_{i=1}^{n} R_{i,p}(\xi)\mathbf{P}_i \tag{29}$$

Using the dot to indicate derivatives with respect to $\xi$ to simplify notation, the Jacobian of the transformation from the Cartesian coordinate system to the parametric space becomes

$$J(s)=\dot{s}=\sqrt{\dot{x}_1^2+\dot{x}_2^2}, \tag{30}$$

and the radius of the beam

$$R(s)=\frac{J^3}{\left|\dot{x}_1\ddot{x}_2-\ddot{x}_1\dot{x}_2\right|}. \tag{31}$$

The unknown displacements and rotations are approximated using the same basis functions as those that are used to describe the geometry:

$$u_t(\xi)\approx\sum_{i=1}^{n} R_{i,p}(\xi)u_t^i; \qquad u_n(\xi)\approx\sum_{i=1}^{n} R_{i,p}(\xi)u_n^i; \qquad \theta_b(\xi)\approx\sum_{i=1}^{n} R_{i,p}(\xi)\theta_b^i. \tag{32}$$

In the parametric space the strains now become

$$\varepsilon_m(\xi)=\frac{\dot{u}_t}{J}-\frac{u_n}{R}, \tag{33}$$

$$\gamma_s(\xi)=\frac{u_t}{R}+\frac{\dot{u}_n}{J}-\theta_b, \tag{34}$$

$$\chi_b(\xi)=\frac{\dot{\theta}_b}{J}. \tag{35}$$

Substituting equations (32) to (35) in total potential energy equation and taking the second derivative of the strain energy $U$ and the first derivative of the potential energy $V$ with respect to the displacement and rotation control points will result in the stiffness matrix and force vector respectively. The integrals are computed using Gaussian quadrature at the knot span level. The unknown displacements and rotations are found by simply solving $\mathbf{Ku}=\mathbf{f}$ and substituting the control point values in equation (32).

When the geometry is more complex and cannot be described by a single NURBS patch, multiple patches have to be created and connected to each other. All the patches are interpolatory at the start and end of the curve, simplifying the process of connecting them. In the present work a master-slave technique is used to make sure the patches are connected properly and the redundant slave degrees of freedom are eliminated. The approach also allows connecting patches through hinges by only matching the displacement degrees of freedom between two patches and leaving the rotation degree of freedom as it is.

### 2.3.2 Global formulation

To obtain a structural model in a global frame of reference some straightforward changes have to be made to the model described in the previous section. The tangential and normal displacements from the local coordinate system are expressed in the global *x* and *y* displacements:

$$u_t(\xi) = \mathbf{u}_g(\xi) \cdot \mathbf{t}(\xi); \qquad u_n(\xi) = \mathbf{u}_g(\xi) \cdot \mathbf{n}(\xi), \tag{36}$$

where $\mathbf{u}_g$ is a vector with *x* and *y* displacements *u* and *w*, and **t** and **n** are the local tangential and normal vectors, respectively. These unit vectors are derived from the NURBS curve describing the geometry:

$$\mathbf{t} = \begin{bmatrix} \dfrac{\dot{x}_1}{J} \\ \dfrac{\dot{x}_2}{J} \end{bmatrix}; \qquad \mathbf{n} = \begin{bmatrix} -t_2 \\ t_1 \end{bmatrix} \tag{37}$$

Substituting equation (36) into the strain equations (33) to (35), results in the strains in a global coordinate system:

$$\varepsilon_m(\xi) = \frac{\dot{\mathbf{u}}_g \cdot \mathbf{t} + \mathbf{u}_g \cdot \dot{\mathbf{t}}}{J} - \frac{\mathbf{u}_g \cdot \mathbf{n}}{R}, \tag{38}$$

$$\gamma_s(\xi) = \frac{\mathbf{u}_g \cdot \mathbf{t}}{R} + \frac{\dot{\mathbf{u}}_g \cdot \mathbf{n} + \mathbf{u}_g \cdot \dot{\mathbf{n}}}{J} - \theta_b, \tag{39}$$

$$\chi_b(\xi) = \frac{\dot{\theta}_b}{J}, \tag{40}$$

The derivatives of the unit tangent and normal vectors are equal to

$$\dot{\mathbf{t}} = \begin{bmatrix} \dfrac{\ddot{x}_1}{J} - \dfrac{\dot{x}_1 \dot{J}}{J^2} \\ \dfrac{\ddot{x}_2}{J} - \dfrac{\dot{x}_2 \dot{J}}{J^2} \end{bmatrix}; \qquad \dot{\mathbf{n}} = \begin{bmatrix} -\dot{t}_2 \\ \dot{t}_1 \end{bmatrix}, \tag{41}$$

where the derivative of the Jacobian can be found with equation (42):

$$\dot{J} = \frac{\dot{x}_1 \ddot{x}_2 + \ddot{x}_1 \ddot{x}_2}{J} \tag{42}$$

The global displacements are again approximated by the NURBS basis functions:

$$u(\xi) \approx \sum_{i=1}^{n} R_{i,p}(\xi) u^i; \qquad w(\xi) \approx \sum_{i=1}^{n} R_{i,p}(\xi) w^i \tag{43}$$

The stiffness matrix and force vector in the global coordinate system can now be found by taking the second derivative with respect to the displacements and rotations of the strain energy and the first derivative with respect to the displacements and rotations of the potential energy of the externally applied forces.

### 2.4 Coupling

The aerodynamic and structural model are loosely coupled, so that both models can use an optimized mesh for the specific analysis and the models can easily be modified/upgraded. [23] The transfer of loads and displacements of the non-matching meshes is done using the $L^2$-projection method as described in Bazilevs et al.[3]

To simplify the problem of data transfer between the models, the aerodynamic geometry is considered to be the master geometry. The structural model is derived from the master geometry by inserting knots to break up the curve into multiple patches, enabling the addition of extra structural elements in the interior of the airfoil. The parametric space for the fluid-structure interface is thus the same for both the aerodynamic and structural model. As a consequence, the value of a function in a certain parametric point on one mesh is equal to the value of this function in the same parametric point on the other mesh.

The pressure $p$, for example, is calculated in the aerodynamic model and has to projected onto the structural mesh:

$$p_s(\xi) = \Pi_s p_a(\xi) \tag{44}$$

meaning that $p_s$ is an $L^2$-projection of $p_a$ onto the space of basis functions defined on the structural mesh. The projection can be written as

$$\int_{\Gamma_s} R^s_{i,p} p_s \, d\Gamma = \int_{\Gamma_s} R^s_{i,p} p_a \, d\Gamma, \tag{45}$$

where $\Gamma$ is the fluid-structure interface mesh. The pressure on the structural mesh can also be approximated using the NURBS basis functions:

$$\int_{\Gamma_s} R^s_{i,p} \sum_{j=1}^{n_s} R^s_{j,p} p^i_s \, d\Gamma = \sum_{j=1}^{n_s} \int_{\Gamma_s} R^s_{i,p} R^s_{j,p} \, d\Gamma p^i_s = \int_{\Gamma_s} R^s_{i,p} p_a \, d\Gamma \tag{46}$$

where $p_s^i$ is the $i^{th}$ control point of the NURBS curve approximating the pressure on the structural mesh. These integrals can simply be computed using Gaussian quadrature. Solving equation (46) for the pressure control points finalizes the transfer of the function from one mesh to the other. The same routine can also be used to transfer the displacements from the structural to the aerodynamic mesh.

## 3 MORPHING AIRFOIL OPTIMIZATION

The aeroelastic framework described in the previous section is applied to the optimization of an active morphing airfoil. The goal is to morph the baseline airfoil shape, designed for optimal performance during cruise flight, into an airfoil shape more suitable for landing conditions. This means that the lift coefficient of the airfoil at a certain angle of attack needs to be maximized resulting in a reduced minimum landing speed and thus increased landing performance. In section 3.1 a description is given for the design case, including the UAV under consideration and the flight conditions of interest to the optimization problem. Section 3.2 covers the setup of the optimization problem. The objective, constraints and design variables will be presented.

### 3.1 Design case

The UAV that is considered for the optimization has a mass of 25kg and its wings are rectangular with the NACA 2412 airfoil. The wingspan is 3.0m and the chord length is 0.6m. The cruise and landing flight conditions are listed in Table 1.

| | | **Cruise** | **Landing** |
|---|---|---|---|
| **Speed** | [km/h] | 110.00 | 56.02 |
| **Altitude** | [m] | 304.8 | 304.8 |
| **Angle of attack** | [°] | - | 6.373 |
| **Lift coefficient** | [-] | 0.2425 | - |

Table 1: Flight conditions for UAV in cruise and landing flight

The internal structure of the airfoil consists of a stiff wing box in the leading edge, with a single spar at 25.00% of the chord. The actuators are located at 43.75%, 62.50% and 81.25% of the chord and have a vertical orientation in the undeformed NACA2412 airfoil. The actuators are connected to the skin through hinges. An illustration of the structure is shown in Figure 3.

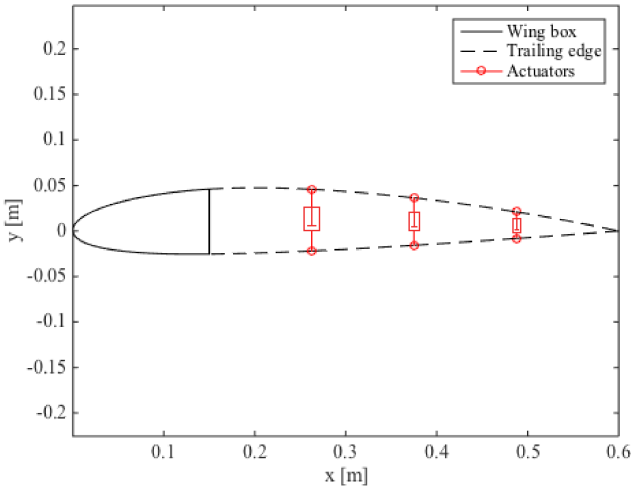

Figure 3: Geometry and internal structure of the morphing airfoil

### 3.2 Optimization setup

The main objective of the optimization is to maximize the lift coefficient in landing flight conditions, while the NACA2412 geometry is maintained during other flight conditions. Two separate analysis runs are done. One at landing conditions with the actuators enabled and one at 2.5g flight conditions with the actuators locked. Additional constraints are added to ensure a feasible design is found:

- Strain constraints are used for the airfoil skin in the morphing section. The IGA framework allows easy strain evaluations at any point on the geometry. In the present work the strain at 100 evenly spaced points were taken into account as constraints. The maximum allowed strain is 4000 microstrain.
- Constraints on the maximum actuation forces and maximum actuator strokes are implemented to avoid infeasible actuator requirements. The maximum value for the

actuation force is set to 500N and the actuator stroke may be at most 40% of the initial length.

- When lamination parameters are included as design variables a set of constraint equations is implemented to ensure feasible laminate designs.

Besides the lamination parameters, the thickness and actuation forces are also included as design variables. The lamination parameters, however, deviate from the standard lamination parameters, because the current framework only covers two-dimensional problems. A modified set of lamination parameters is used to scale the membrane and bending stiffness of the laminate: [24]

$$EI = \alpha \frac{wh^3 E_{ref}}{12}, \tag{47}$$

$$EA = \beta wh E_{ref}, \tag{48}$$

where $h$ and $w$ are the thickness and width of the laminate, and $E_{ref}$ is the reference Young's modulus of the material. In the current work the modulus in the fiber direction of the material used in the optimization, carbon fiber AS4/8773, was selected as the reference Young's modulus. The specifications of the material are given in Table 2.

| | | **AS4/8773** |
|---|---|---|
| **$E_1$** | [N/m$^2$] | $1.198 \cdot 10^{11}$ |
| **$E_2$** | [N/m$^2$] | $9.08 \cdot 10^{9}$ |
| **$G_{12}$** | [N/m$^2$] | $5.29 \cdot 10^{9}$ |
| **ν** | [-] | 0.32 |
| **$t_{ply}$** | [mm] | $1.83 \cdot 10^{-4}$ |

Table 2: Material properties of carbon fiber AS4/8773

A set of boundaries for the feasible design space was found by simply checking many different laminates and take the outer boundaries of the dataset. For unidirectional pre-impregnated carbon fiber in an epoxy material AS4/8773 the bounding box is created by the following equations:

$$\begin{aligned}
-\beta_i + 0.474\alpha_i + 0.0368 \le 0, &\quad \text{for } i = 1 \ldots N_p \\
\beta_i - 1.3013\alpha_i + 0.5656 \le 0, &\quad \text{for } i = 1 \ldots N_p \\
\beta_i - 9.4808\alpha_i + 8.4808 \le 0, &\quad \text{for } i = 1 \ldots N_p \\
-\beta_i + 0.4694\alpha_i + 0.5306 \le 0, &\quad \text{for } i = 1 \ldots N_p \\
-\beta_i + 1.2842\alpha_i + 0.2476 \le 0, &\quad \text{for } i = 1 \ldots N_p \\
\beta_i - 8.9981\alpha_i + 0.5595 \le 0, &\quad \text{for } i = 1 \ldots N_p
\end{aligned} \tag{49}$$

The design space of a laminate with fewer layers is conservative with respect to the design spaces of a laminate with more layers, so a minimum thickness can be chosen and the design space for this thickness can be safely used for thicker lamina as well.

The globally convergent method of moving asymptotes (GCMMA) is used to perform the gradient-based optimization. [25] The gradients are computed analytically, ensuring efficient and accurate sensitivities. The Karush-Kuhn-Tucker optimality conditions are used as convergence criterion.

Four different optimization cases are studied in the present work. First of all, a baseline optimization is done where only the actuation forces are included as design variables. The thickness for the baseline is chosen such that the cruise geometry can still be closely maintained during the 2.5g load case and is equal to 20 plies, or 3.66mm. The laminate is set to a quasi-isotropic one by setting the lamination parameters to 0.5. The second optimization also includes the thickness of the skin as design variable besides the actuation forces. The third case uses the actuation forces and lamination parameters to obtain an optimal result. The final optimization includes all the design variables and should theoretically give the best result. Table 3 gives and overview of the settings per optimization case.

| # | | **Skin thickness** | **Actuation forces** | **Lamination parameters** |
|---|---|---|---|---|
| 1 | Baseline | 3.66 mm | Free | $\alpha = \beta = 0.5$ |
| 2 | Thickness | Free | Free | $\alpha = \beta = 0.5$ |
| 3 | Laminate | 3.66 mm | Free | Free |
| 4 | Thickness + laminate | Free | Free | Free |

Table 3: Settings for the four optimization cases

## 4 RESULTS

The results of the four separate optimization cases are presented in this section. First the baseline result is presented to understand what the performance of a non-optimized structure would be. The results of the other optimization cases are compared with the baseline, but also with each other. Finally, the effect of viscosity on the results is discussed.

### 4.1 Baseline

The resulting deformed shape with the constant skin thickness and quasi-isotropic layup is shown in Figure 4, together with the undeformed shape and actuator connection points.

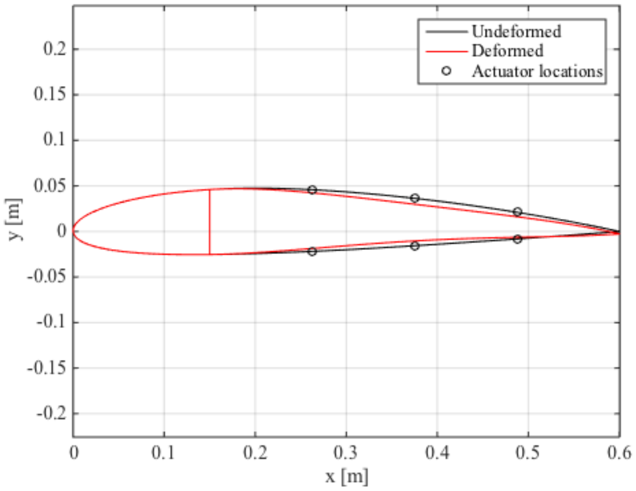

Figure 4: Baseline deformed and undeformed shape in landing flight conditions

It is visible that the thickness of the trailing edge is decreased and the camber is slightly increased, which indeed results in an increase in lift coefficient. In undeformed landing configuration the lift coefficient is equal to 1.025 and for the deformed configuration a coefficient of 1.069 is found.

Because the thickness and lay-up is uniform throughout the skin, the deformation is almost symmetric. The actuation force in this case limits the deformation. All three actuation force design variables are hitting their upper limit of 500N, preventing the optimizer to move towards more extreme camber lines. None of the other constraints are active. The cruise shape is maintained during the 2.5g load case.

### 4.2 Skin thickness optimization

Figure 5 shows the deformed shape resulting from the skin thickness optimization. The actual skin thickness distribution is shown in Figure 6, where also the skin thickness of the baseline structure is shown for comparison.

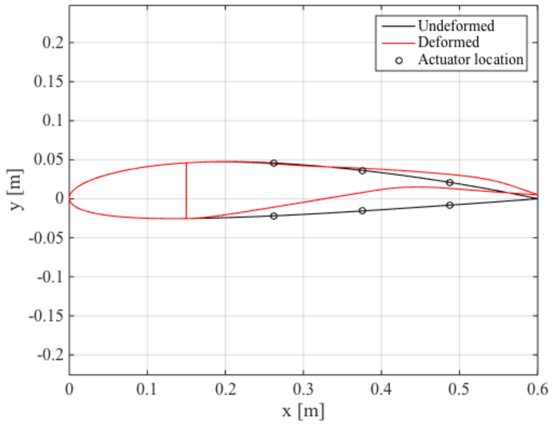

Figure 5: Thickness optimization resulting deformation

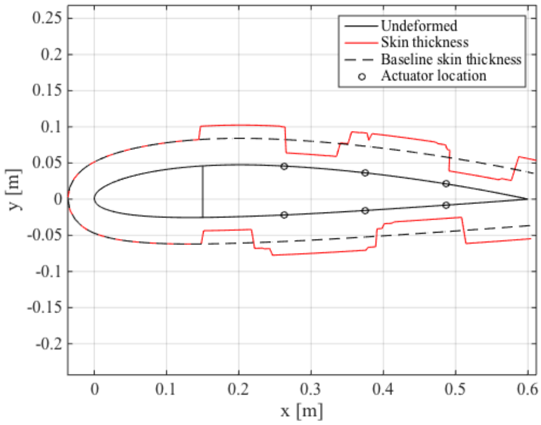

Figure 6: Thickness optimization resulting thickness distribution

The variation in skin thickness allows the optimizer to introduce more camber compared to the baseline result. This results in an increased lift coefficient of 1.303, which is significantly higher than the undeformed result.

The thickness distribution shows that most of the thickness design variables are at their limit values. The thickness of the skin connected to the spar at the bottom side has the lowest thickness possible to introduce a compliant hinge. At the top the opposite is observed. The thickness is increased to the maximum value in order to maintain a stiff connection in this location. This allows for more camber to be introduced in the structure.

The middle and last actuators are at their maximum stroke and force and the strain constraint is active at the bottom of the spar. In the other thin sections the strain is approaching, but not hitting the upper limit. The cruise shape is again maintained during the 2.5g load case.

### 4.3 Laminate optimization

The skin deformation and lamination parameters for the laminate optimization case are shown in Figure 7, and Figure 8 and Figure 9, respectively. The deformation is again larger compared to the baseline, but less severe compared to the thickness optimization case. This is also reflected in the resulting lift coefficient of 1.244, which is in between the baseline and thickness optimization values.

The lamination parameters both show similar behavior as the thickness distribution in the previous case. The stiffness is strongly reduced and increased in same sections as where the thickness was reduced and increased in the previous results. The thickness, however, has a larger influence on the bending stiffness, explaining the better result for the skin thickness optimization.

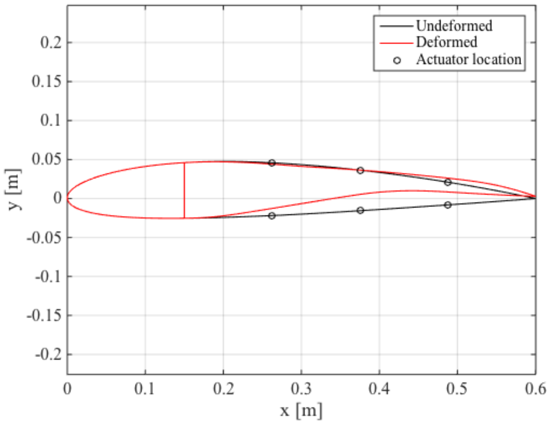

Figure 7: Laminate optimization resulting deformation

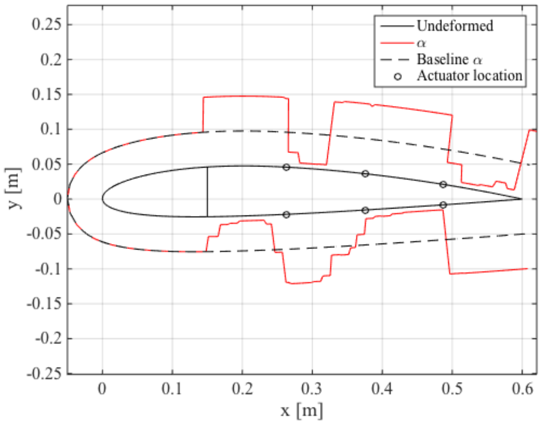

Figure 8: Laminate optimization resulting α distribution

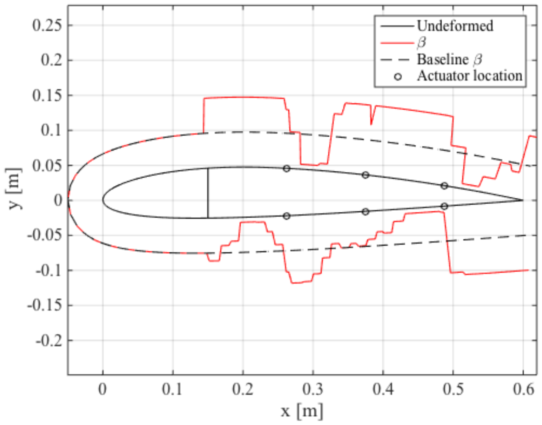

Figure 9: Laminate optimization resulting β distribution

Similar as to the previous results, the middle and last actuator reach their maximum stroke and force. The strain limit is now reached in in all thin sections. The cruise shape is maintained during the 2.5g load case.

### 4.4 Skin thickness and laminate optimization

A kink can be recognized towards the end to the airfoil in the resulting deformation for the case with both skin thickness and lamination parameters as design variables that is shown in Figure 10. This flap-like deformation increases the lift coefficient even more compared to the skin thickness optimized result. A lift coefficient of 1.419 is found.

The optimized design variables are displayed in Figure 11 to Figure 13 and show again similar behavior as the previous results. The distinction between the stiffer and more flexible sections is less clear for the membrane stiffness design variable, but this is due to the low impact of the membrane stiffness on the result. The deformation of the structure is bending dominated, causing the membrane stiffness variables to converge more slowly.

The middle and last actuator reach the limit of the stroke again, but for the actuator force there is a difference compared to the previous results. Whereas in the previous results the first actuator applied a force of around 300N, in this case the actuator only applies 35N. This is most likely caused by the fact that both α and the thickness are low in the bottom section before the first actuator. The required force to bend the bottom skin is therefore significantly lower compared to the previous results. The strain limit is again reached in the more flexible sections. Again the cruise shape is maintained during the 2.5g load case.

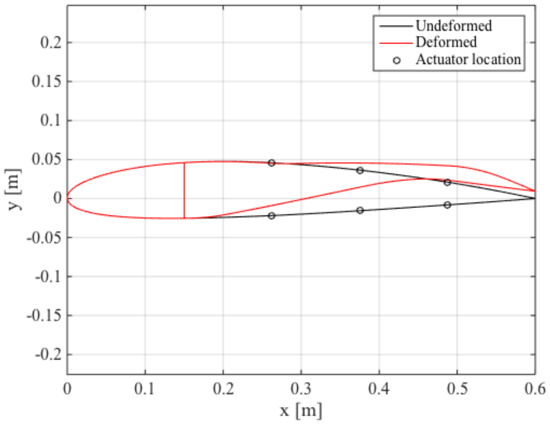

Figure 10: Thickness and laminate optimization resulting deformation

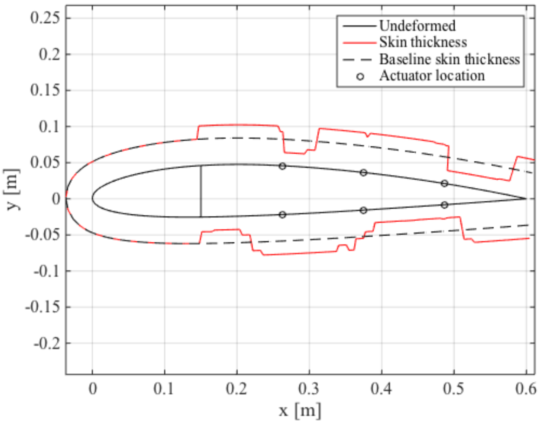

Figure 11: Thickness and laminate optimization resulting thickness distribution

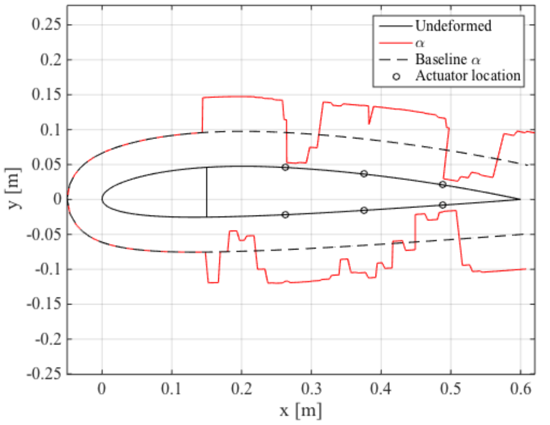

Figure 12: Thickness and laminate optimization resulting α distribution

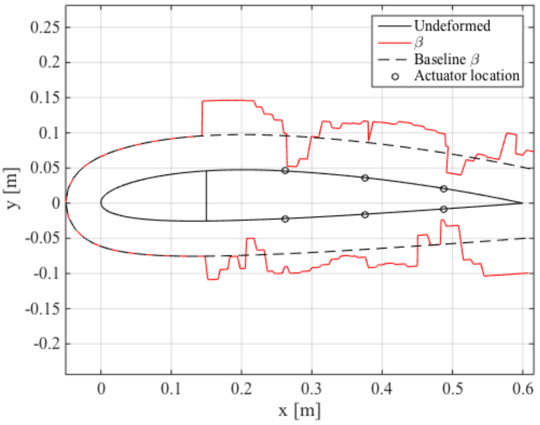

Figure 13: Thickness and laminate optimization resulting β distribution

## 4.5 Viscous effects

In the presented framework an inviscid aerodynamic model is used in the aeroelastic calculations. Effect like viscous drag, boundary layer thickness and flow separation are currently not taken into account, even though these phenomena can have significant influence on the resulting aerodynamic performance. Especially at higher angles of attack and lower Reynolds numbers this has to be taken into account. To check the validity of the results, the resulting airfoil shapes are also analyzed using Xfoil. [26] The results of these simulations are listed in Table 4.

| | Inviscid lift coefficient [-] | Viscous lift coefficient [-] |
|---|---|---|
| **NACA2412** | 1.025 (-) | 0.937 (-) |
| **Baseline** | 1.069 (4.3%) | 0.983 (4.9%) |
| **Thickness** | 1.303 (27.1%) | 1.051 (12.2%) |
| **Laminate** | 1.244 (19.4%) | 1.038 (10.8%) |
| **Thickness + laminate** | 1.419 (38.4%) | 1.024 (9.3%) |

Table 4: Inviscid and viscous lift coefficients for the NACA 2412 airfoil and the optimized deformed airfoil shapes and the percentage of increase compared to the NACA2412 airfoil

These results show that viscosity has a large influence on the lift coefficients of the optimized airfoils. For the NACA2412 and baseline the lift coefficient reduces by 8 to 9%, whereas for the other airfoils the reduction can go up to 28% for the case with all the design variables included in the optimization. Looking closer into the boundary layer variables shows that for this case separation occurs just before the very end of the trailing edge. This separation is caused by the sharp kink at the topside of the trailing edge towards the end. The flow has difficulties to stay attached after the kink, even at lower angles of attack. This explains the large reduction in lift coefficient for this design.

The other airfoil shapes do not show separation, because this sharp kink is not present in these solutions. The boundary layer thickness, however, has significant influence on the pressure distribution. Compared to the NACA2412 there is still a significant increase for the viscous lift coefficient of up to 12.2%. The results do show, however, that for this kind of aeroelastic stiffness/shape optimization a more detailed aerodynamic model would result in more reliable designs.

## 5 CONCLUSIONS

A two-dimensional low-fidelity isogeometric aeroelastic optimization framework was presented and applied to the optimization of an active morphing airfoil. The framework consists of an isogeometric BEM potential flow solver and an isogeometric curved Timoshenko beam solver, which are loosely coupled. Both solvers make use of NURBS basis functions to describe the geometry and approximate the unknown variables. The data transfer between the models is carried out through $L^2$-projections of the pressure and displacement functions from one mesh to the other.

The integrals for the aerodynamic model are desingularized, enabling easy calculation of the originally singular contributions to the aerodynamic influence coefficients. The multi-patch beam model is formulated in a global frame of reference to simplify the data transfer. The patches are connected through a master slave technique, enable both rigid connections and hinged connections.

The aeroelastic optimization framework was used to optimize the landing performance of a 25kg UAV. The airfoil shape for cruise conditions was set to a NACA2412 and the goal was to maximize the lift coefficient during landing flight conditions by adding three actuators in the trailing edge of the airfoil and optimizing the skin thickness and lamination parameters. Four cases were optimized with varying design variables.

The results showed that higher lift coefficients were achieved, as more design variables were included, as was expected. The skin thickness was shown to be the most important design variable in the presented design case, because the structure is predominantly loaded in bending. The inviscid results showed an increase in lift coefficient of up to 38% for the case with both skin thickness and lamination parameter as design variables.

Viscous results obtained using Xfoil showed that the benefits were overestimated. The flap-like deformation of the most promising design caused flow separation, resulting in a significantly lower lift coefficient. The other design did not suffer from flow separation, but the effect of the boundary layer was clearly noticeable in these cases as well. The increase in lift coefficient reduced to 10.8% for the design with optimized skin thickness.

## 6 REFERENCES

[1] Hughes, T.J.R., Cottrell, J.A., Bazilevs, Y., Isogeometric analysis: CAD, finite elements, NURBS, exact geometry and mesh refinement. *Computer Methods in Applied Mechanics and Engineering* 2005, *194*, 4135–4195.

[2] Bazilevs, Y., Hsu, M.-C., Kiendl, J., Wüchner, R., et al., 3D simulation of wind turbine rotors at full scale. Part II: Fluid–structure interaction modeling with composite blades. *International Journal for Numerical Methods in Fluids* 2011, *65*, 236–253.

[3] Bazilevs, Y., Hsu, M.-C., Scott, M.A., Isogeometric fluid–structure interaction analysis with emphasis on non-matching discretizations, and with application to wind turbines. *Computer Methods in Applied Mechanics and Engineering* 2012, *249–252*, 28–41.

[4] Korobenko, A., Hsu, M.-C., Akkerman, I., Tippmann, J., et al., Structural mechanics modeling and fsi simulation of wind turbines. *Mathematical Models and Methods in Applied Sciences* 2012, *23*, 249–272.

[5] Bazilevs, Y., Calo, V.M., Zhang, Y., Hughes, T.J.R., Isogeometric Fluid–structure Interaction Analysis with Applications to Arterial Blood Flow. *Computational Mechanics* 2006, *38*, 310–322.

[6] Bazilevs, Y., Gohean, J.R., Hughes, T.J.R., Moser, R.D., et al., Patient-specific isogeometric fluid–structure interaction analysis of thoracic aortic blood flow due to implantation of the Jarvik 2000 left ventricular assist device. *Computer Methods in Applied Mechanics and Engineering* 2009, *198*, 3534–3550.

[7] Politis, C., Ginnis, A.I., Kaklis, P.D., Belibassakis, K., et al., An Isogeometric BEM for Exterior Potential-flow Problems in the Plane, in: *2009 SIAM/ACM Joint Conference on Geometric and Physical Modeling*, ACM, New York, NY, USA 2009, pp. 349–354.

[8] Takahashi, T., Matsumoto, T., An application of fast multipole method to isogeometric boundary element method for Laplace equation in two dimensions. *Engineering Analysis with Boundary Elements* 2012, *36*, 1766–1775.

[9] Heltai, L., Arroyo, M., DeSimone, A., Nonsingular isogeometric boundary element method for Stokes flows in 3D. *Computer Methods in Applied Mechanics and Engineering* 2014, *268*, 514–539.

[10] Simpson, R.N., Scott, M.A., Taus, M., Thomas, D.C., et al., Acoustic isogeometric boundary element analysis. *Computer Methods in Applied Mechanics and Engineering* 2014, *269*, 265–290.

[11] Li, K., Qian, X., Isogeometric analysis and shape optimization via boundary integral. *Computer-Aided Design* 2011, *43*, 1427–1437.

[12] Simpson, R.N., Bordas, S.P.A., Trevelyan, J., Rabczuk, T., A two-dimensional Isogeometric Boundary Element Method for elastostatic analysis. *Computer Methods in Applied Mechanics and Engineering* 2012, *209–212*, 87–100.

[13] Lian, H., Simpson, R., Bordas, S., Stress analysis without meshing: isogeometric boundary element method. *Proceedings of the ICE - Engineering and Computational Mechanics* 2013, *166*, 88–99.

[14] Cho, S., Ha, S.-H., Isogeometric shape design optimization: exact geometry and enhanced sensitivity. *Structural and Multidisciplinary Optimization* 2008, *38*, 53–70.

[15] Kenway, G.K.W., Martins, J.R.R.A., Multipoint High-Fidelity Aerostructural Optimization of a Transport Aircraft Configuration. *Journal of Aircraft* 2014, *51*, 144–160.

[16] Piegl, L., Tiller, W., The NURBS Book, Springer Science & Business Media, 2012.

[17] Cottrell, J.A., Hughes, T.J.R., Bazilevs, Y., Isogeometric Analysis: Toward Integration of CAD and FEA, John Wiley & Sons, 2009.

[18] Morino, L., Boundary Integral Equations in Aerodynamics. *Applied Mechanics Reviews* 1993, *46*, 445–466.

[19] Klaseboer, E., Fernandez, C.R., Khoo, B.C., A note on true desingularisation of boundary integral methods for three-dimensional potential problems. *Engineering Analysis with Boundary Elements* 2009, *33*, 796–801.

[20] Katz, J., Plotkin, A., Low-Speed Aerodynamics, Cambridge University Press, 2001.

[21] Bouclier, R., Elguedj, T., Combescure, A., Locking free isogeometric formulations of curved thick beams. *Computer Methods in Applied Mechanics and Engineering* 2012, *245–246*, 144–162.

[22] Cazzani, A., Malagù, M., Turco, E., Isogeometric analysis of plane-curved beams. *Mathematics and Mechanics of Solids* 2014, 1081286514531265.

[23] Farhat, C., Lesoinne, M., Le Tallec, P., Load and motion transfer algorithms for fluid/structure interaction problems with non-matching discrete interfaces: Momentum and energy conservation, optimal discretization and application to aeroelasticity. *Computer Methods in Applied Mechanics and Engineering* 1998, *157*, 95–114.

[24] Thuwis, G.A.A., Stiffness and Layout Tailoring of a Morphing High-lift System with Aeroelastic Loads, Delft University of Technology, 2012.

[25] Svanberg, K., A Class of Globally Convergent Optimization Methods Based on Conservative Convex Separable Approximations. *SIAM Journal on Optimization* 2002, *12*, 555–573.

[26] Drela, M., XFOIL: An Analysis and Design System for Low Reynolds Number Airfoils, in: Mueller, T.J. (Ed.), *Low Reynolds Number Aerodynamics*, Springer Berlin Heidelberg, 1989, pp. 1–12.

## COPYRIGHT STATEMENT